

# Dipole orientation reveals single-molecule interactions and dynamics on 2D crystals

Wei Guo<sup>1</sup>, Tzu-Heng Chen<sup>1,\*</sup>, Nathan Ronceray<sup>1</sup>, Eveline Mayner<sup>1</sup>, Kenji Watanabe<sup>2</sup>, Takashi Taniguchi<sup>2</sup>, Aleksandra Radenovic<sup>1,\*</sup>

<sup>1</sup> *Laboratory of Nanoscale Biology, Institute of Bioengineering (IBI), School of Engineering (STI), École Polytechnique Fédérale de Lausanne (EPFL), Lausanne, Switzerland.*

<sup>2</sup> *Research Center for Materials Nanoarchitectonics, National Institute for Materials Science, Tsukuba, Japan*

\* Email: [tzu-heng.chen@epfl.ch](mailto:tzu-heng.chen@epfl.ch), [aleksandra.radenovic@epfl.ch](mailto:aleksandra.radenovic@epfl.ch)

## Abstract

Direct observation of single-molecule interactions and dynamic configurations in situ is a demanding challenge but crucial for both chemical and biological systems. However, optical microscopy that relies on bulk measurements cannot meet these requirements due to rapid molecular diffusion in solutions and the complexity of reaction systems. In this work, we leveraged the fluorescence activation of pristine hexagonal boron nitride (h-BN) in organic solvents as a molecular sensing platform, confining the molecules to a two-dimensional (2D) interface and slowing down their motion. Conformational recognition and dynamic tracking were achieved simultaneously by measuring the 3D orientation of fluorescent emitters through polarized single-molecule localization microscopy (SMLM). We found that the orientation of in-plane emitters aligns with the symmetry of the h-BN lattice, and their conformation is influenced by both the local conditions of h-BN and the regulation of the electrochemical environment. Additionally, lateral diffusion of fluorescent emitters at the solid-liquid interface displays more abundant dynamics compared to solid-state emitters. This study opens the door for the simultaneous molecular conformation and photophysics measurement, contributing to the understanding of interactions at the single-molecule level and real-time sensing through 2D materials.

## Keywords

2D materials, dipole orientation, light polarization, single-molecule localization microscopy.

# 1. Introduction

Single-molecule tracking and conformational dynamics measurement are essential for understanding both chemical reactions<sup>1-4</sup> and biological systems<sup>5-7</sup>. However, the diffusion coefficients of molecules in solution far exceed the temporal resolution of optical microscopy<sup>4,8</sup>, and the complex structures of the molecules make it challenging to infer their equilibrium configuration in the far field<sup>5,9,10</sup>. As a result, recent studies have increasingly focused on the interaction and confinement of hexagonal boron nitride (h-BN) with single molecules<sup>11-16</sup>, because of its remarkable mechanical strength, atomically flat surface and the ability to slow down the diffusion movement<sup>13,15,17,18</sup>. The wide band gap of h-BN makes it compatible with fluorescence imaging at its surface compared to graphene and MoS<sub>2</sub> substrates<sup>19-21</sup>. Additionally, surface defects on h-BN play a critical role not only in solid-state quantum emitters<sup>22,23</sup> but also in probing molecular coupling and sensing at solid-liquid interfaces in nanofluidics<sup>17,18</sup>. Techniques such as irradiation exposure<sup>24-26</sup>, doping<sup>27,28</sup>, annealing<sup>29,30</sup>, and etching<sup>31,32</sup> already activate the optical properties of h-BN defects in solid-state applications. Moreover, the activation of quantum emission from defects could also be induced in the solvent environment through plasma treatment<sup>17,18</sup> and the chemisorption of organic molecules on the h-BN surface<sup>13</sup>.

To understand the photophysics of these quantum emitters in realistic environments with high throughput<sup>33-35</sup>, interactions between molecules and pristine h-BN can be studied by single-molecule localization microscopy (SMLM). While conventional SMLM only provides information about the intensity and localization of the emitters, comprehensive profiling demands additional properties such as spectrum<sup>33,36,37</sup>, polarization<sup>38-41</sup>, and lifetime<sup>42-44</sup>. In this case, the investigation of 3D orientations of emission dipoles has been a subject of interest in both physics and biology research<sup>7,45,46</sup>. This interest stems from the compatibility with SMLM without sacrificing temporal and spatial resolution, and it has developed many approaches including pupil splitting<sup>47-52</sup>, back focal plane modulation<sup>53-55</sup>, and excitation modulation<sup>45,56</sup>. Although these methods have been employed to study heterogeneities in biological systems, the precise relationship between dipole orientations, molecular configurations, and emitter dynamics remains unclear due to biological complexity.

In this study, we utilize polarized SMLM to map the nanoscale localization and track the 3D orientation of fluorescent emitters, correlating their orientation and conformation with the h-BN crystal precisely in the acetonitrile solvent. Our findings reveal that molecular interactions at the liquid-solid interface are regulated by both the crystal structure of h-BN and the electrochemical condition, providing new insights into the dynamic behavior of molecules in complex surface environments.

## 2. Results

### 2.1 Experimental concept and optical activity of fluorescent emitters

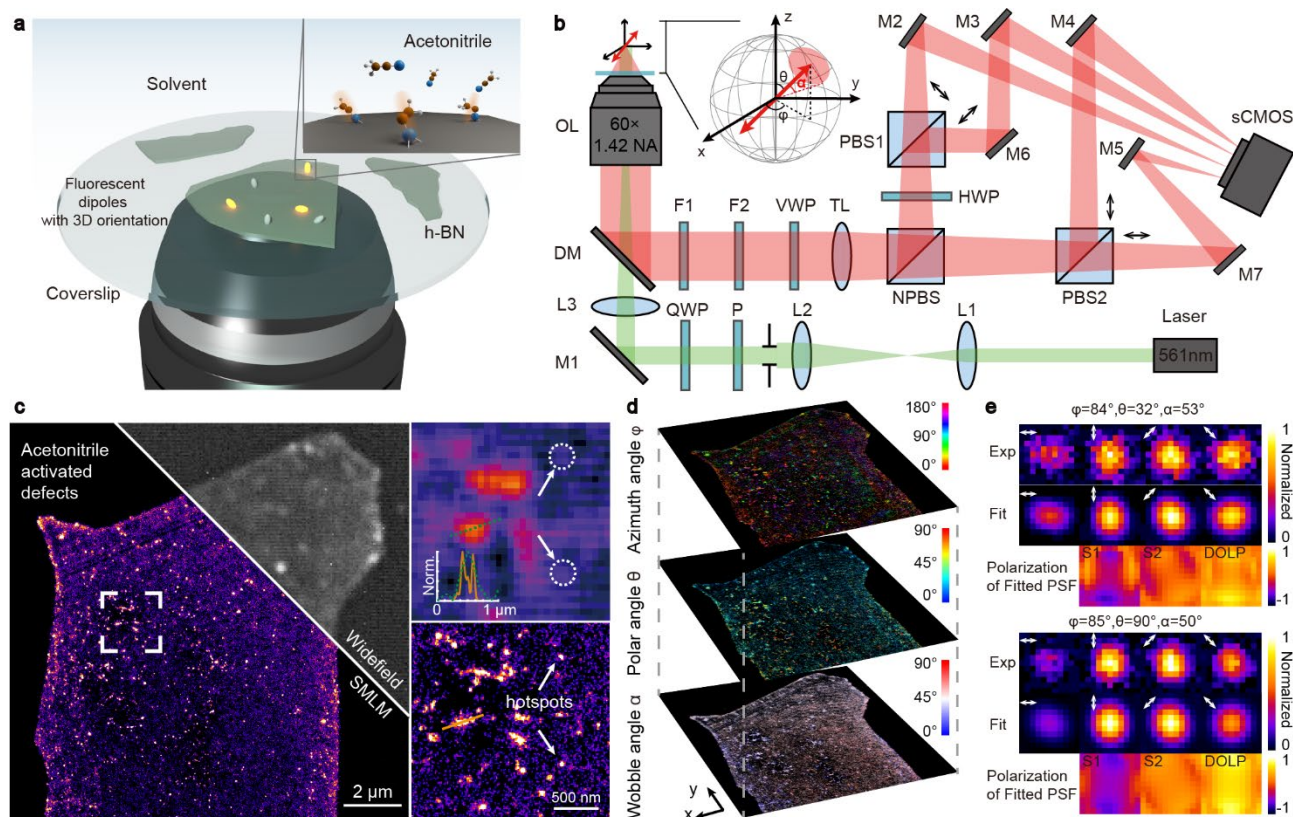


**Fig. 1 Optical activity of emitters at h-BN surface.** (a) Rendering of the molecular probing principle. The small figure shows the concept of dipole orientation because of the molecular deformation. (b) The schematic diagram of polarized single-molecule localization microscopy (SMLM) setup. L1-L3: lens; P: polarizer; QWP: quarter waveplate; M1-M7: mirror; OL: objective lens; DM: dichroic mirror; F1-F2: filter; VWP: variable waveplate; TL: tube lens; NPBS: non-polarizing beamsplitter; PBS1-PBS2: polarizing beamsplitter; HWP: half waveplate. (c) The comparison of SMLM and widefield images. The SMLM records more interaction activity and displays them as hotspots. (d) Super-resolution rendering of the 3D angular parameters of the emitters, which demonstrates their activity and preference on the h-BN surface. (e) Two representative PSFs with large wobble angles. From top to bottom are the experimental results, fitted results, and polarization (Stokes vectors and degree of linear polarization).

To observe non-invasively the optical activity of the h-BN surface in response to the nanoscale environment<sup>13,17,18</sup>, the h-BN flakes are exfoliated from the high-quality crystals to the coverslip and immersed in organic solvent. We chose acetonitrile as the ambient condition due to its linear geometry, without tautomer, and highest purity (>99.9%) among commercial organic solvents. The whole sample is then placed in a homemade holder and fixed on the inverted microscope (Fig. 1a). The 561 nm laser is chosen as an excitation beam and the non-fluorescent h-BN flakes produce

quantum emitters at the liquid-solid interface. The averaged spectrum of these emitters is 600-700 nm with a zero-phonon line peak near 635 nm<sup>13,57</sup>, but it is still challenging to interpret the behavior of each emitter based on this averaged characteristic. These optically activated and sparsely dispersed blinking emitters are presented as diffraction-limited point spread functions (PSF) with excellent photon budgets, making them suitable for analysis with single-molecule localization microscopy in the range of nanometers.

In general, the PSFs would be approximated as 2D Gaussian models, but more information can be extracted through polarization measurements because of the role of transition dipole moments in fluorescence. The orientation and rotational behavior of the emission dipole generated from the interaction of solvent molecules and native defect of h-BN can be probed through the optical microscopy. Here we chose the four-pupil-splitting polarized-SMLM<sup>48-50</sup> as shown in Fig. 1b, which is a trade-off between camera acquisition time (number of photons) and localization accuracy. This strategy has the best azimuthal accuracy<sup>58,59</sup> and excellent photon budget tolerance (typical value is 50 ms for sCMOS in this work) compared to other PSF engineering methods (>100-200 ms for commercial fluorescent dyes). To meet the needs of molecular dynamics studies at the millisecond scale, in this work, we also extend it to orientation measurements of the azimuth ( $\varphi$ ), polar ( $\theta$ ), and wobble angles ( $\alpha$ ) of emission dipoles based on the rotational dipole model<sup>60,61</sup> (**Supplementary section 1**). The fluorescence from the dipoles (red path) is divided by three beam splitters into four channels with different linear polarization states: 0°, 90°, 45°, and 135° separately. Subsequently, four polarized PSFs from the same emission dipole are recorded simultaneously by a single camera and the simulated annealing algorithm is employed to estimate the 3D orientation by iterating a loss function involving the PSFs and degree of linear polarization (DoLP) map (**Supplementary section 2.1**).

h-BN is atomically flat and has a 6eV band gap that cannot be directly excited by visible light. While the same is true for the organic molecules, carbon or oxygen doping could modulate the band gap, providing the prerequisites for h-BN to produce solid-state quantum emitters<sup>27,28</sup>. Therefore, combining the above two points, the chemisorption of organic molecules to the defects on the h-BN surface provides the potential to reduce the bandgap through hybrid with defect state and additionally allow strong fluorescence in visible range<sup>13</sup>. Fig. 1c shows the super-resolved reaction sites of the liquid-activated emitters on the h-BN surface in high throughput and the nanoscale resolution of SMLM compared to widefield in the zoomed-in diagram. The imaging strategy is similar to point accumulation in nanoscale topography (PAINT), where the transient binding and leaving of organic molecules with defects generate a series of single-molecule fluorescence signals. After these fluorescent PSFs are accurately localized, the brightness of the hot spot in the SMLM represents the number of frames occurring at that location, and the higher the activation frequency, the brighter it

becomes (Fig. 1c). Furthermore, these discrete hotspots are spread throughout the entire flake, so the size of these clusters is related to the surface energy of the preferred positions to attract molecules, and it determines the resolution of the SMLM image ( $\sim 30$  nm in this work, as estimated by the phase decorrelation<sup>62</sup> in **Supplementary section 3**). Further results on dipole orientation and mobility are shown in Fig. 1d and each parameter can be rendered as a pseudo-color map, showing the ability of the method to reveal wobble, polar, and azimuthal angles. Moreover, Fig. 1e shows two typical experimental polarized-PSFs and their fitting results, for which an empirical interpretation can be stated as follows considering a stationary dipole: The distribution of the light intensity on the four polarization channels will depend on the azimuthal angle, while the presence of the polar angle will lead to shifts and deformations of polarized PSFs. In the case of wobbling dipoles, both features will be degraded. In the following sections we will present a step-by-step description of the molecule-crystal interaction through dipole orientation.

## 2.2 The breaking of axial symmetry reveals the reactivity of molecule-activated emitters

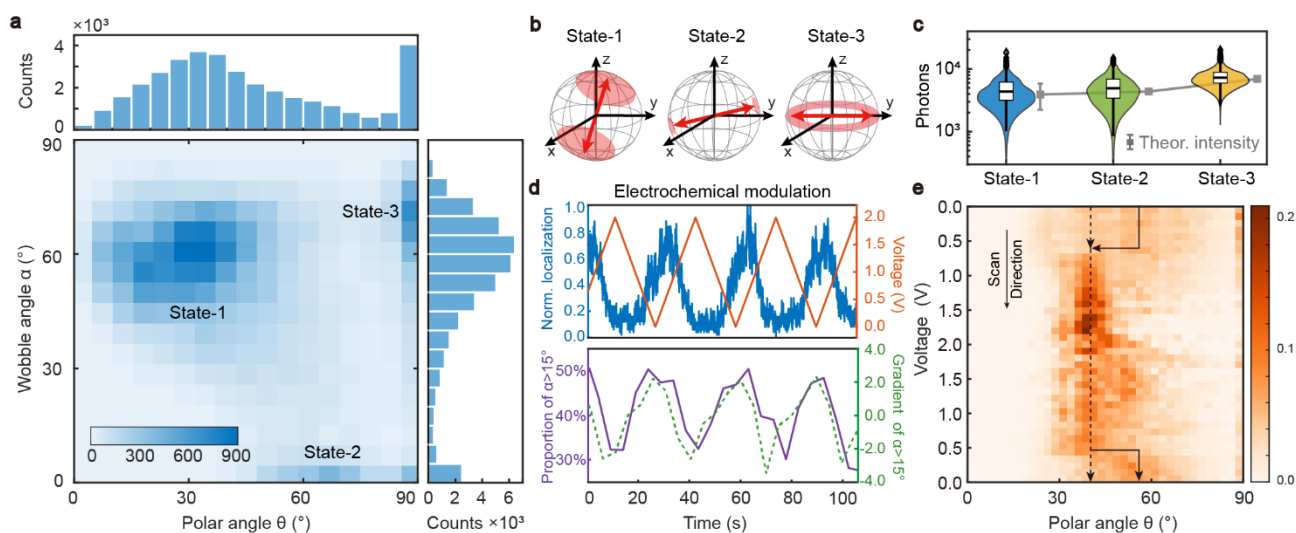


**Fig. 2 Breaking of axial symmetry demonstrates single-molecule interaction with the h-BN surface.** (a) The density map of polar angle vs wobble angle shows three clusters; (b) The arrows indicate the orientations of the three emitter states in spherical coordinates, and the shaded areas indicate the wobbling range; (c) The light intensity histograms of three states, which are in ascending order with the polar angle and agree with the normalized theoretical values; (d) Regulating effect of the vertical potential on the emitters. In the top panel, the orange curve is a triangle wave that is applied to the ITO electrode below the sample (against the Pt electrode) and the blue curve is the normalized localization counts. The bottom panel shows the proportion (violet) and gradient (dash green) of emitters with  $\alpha > 15^\circ$  (i.e. state-1 & state-3) to the total number of localizations under current voltages; (e) Shift on the polar angle of state-2 under the electrochemical modulation. The pixels in each row represent the state-2 histogram at the current voltage.

Directly measuring the structure and dynamics of single-molecule interactions is highly challenging. Here, we propose using emitter orientation to rapidly couple out the state-to-state structural difference. Here, the acetonitrile interaction with h-BN creates fluorescent emission in the visible range through a reversible interaction. Ambient differences among defects is likely responsible for variations in polarization. At a constant power of  $2 \times 10^3 \text{ W/cm}^2$  with circularly polarized laser (ellipticity > 97%) as the excitation light, the ability to extract polar and wobble angles allows us to identify three distinct populations instead of two (Fig. 2a) on a flat crystal where no edges were included. The bin size of the grid is chosen based on numerical simulations of polar-PSFs at different SNRs (**Supplementary section 2.2**), which takes care of overestimating orientational accuracy compared to the Cramer-Rao lower bound. Fig. 2b illustrates the orientation of three states in the spherical coordinate and rotational diffusion in a cone. The first state has the smallest polar angle and allows the dipole to wobble in a large conical region due to thermal fluctuations, etc. The second state is almost parallel and firmly locked to the h-BN surface. The third state is slightly different in that it has a larger wobble angle compared to the first, but the polar angle is nearly  $90^\circ$ . Since the  $C_3$  symmetry of single-atom defect and 2D confinement effect of h-BN, this state suggests that it originates from the binding of organic molecules with rotational mobility, instead of the unrestricted wobbling, at symmetric contact sites on the lattice. Moreover, the angular fluorescence intensity distribution of a fixed emission dipole at the far-field depends on  $\langle \sin(\theta)^2 \rangle$ , so that the light intensity of the three clusters is in ascending order with the polar angle and agrees well with the normalized theoretical value, as reflected in the normalized histograms in Fig. 2c.

Both solid-state quantum emitters and fluorescent dyes are regulated by external conditions<sup>30,57,63,64</sup>, and our situation is no exception. To further understand the dynamics of the interaction and to discuss the effect of chemical structure on photophysical properties, we chose to investigate the effect of changing the electrochemical potential. This has previously been shown to induce large changes in the populations of molecule mediated emitters by inducing neighboring reactions<sup>57</sup>. To further understand the effect on the orientation of emitters we employed a similar electrochemical system while also measuring dynamically the polarization states. Here we use a two-electrode system with a working electrode (indium tin oxide, ITO) and a counter/reference electrode (Platinum, Pt). All potentials are herein reported against the Pt reference. The whole sample was scanned with cyclic voltammetry from 0-2V for 15 cycles to ensure the stability of electrodes and solvent in this working range (**Supplementary section 3**). Fig. 2d shows the change in the number of localizations during the three consecutive cycles. Under the application of an increasingly positive electrochemical potential, the localization (blue curve) decreases (orange curve) and vice versa, which can be observed by all SMLM techniques but cannot be concluded to the molecular structure<sup>57,63</sup>. But when analyzing each set of emitter states separately, we find that the proportion (abbreviated as P, violet curve) of wobble angles  $\alpha > 15^\circ$  (i.e., state-1 & state-3, P1+P3) is consistent with the trend of the

overall number of localizations. In contrast, the proportion of state-2 ( $\alpha < 15^\circ$ ) increases with increasing voltage, suggesting that the stability of the emitter is dependent on state differences.

Under the condition of no voltage applied (Fig. 2a), the value of P1+P3 is larger than 80% and dominates the variation of the overall numbers. However, under the influence of the potential gradient, the share of this fraction is significantly suppressed to less than 50%, indicating that the rotational diffusion correlates with more reactivity and is more sensitive to the environmental conditions than that of the state-2. In terms of temporal dynamics of these emitters, although macroscopic changes in the number of localizations respond to the changing electrochemical environment with a phase delay of a few seconds, the gradient (green) shows that the emitter does respond immediately when the voltage is reversed. Besides, after stacking the histograms of polar angle for state-2 into a 2D heat map (Fig. 2e), the pixel colors in each row indicate the number density at the current potential. Although the structure of state-2 is more stable, it can be noticed that these dipole orientations still shift in the polar angle. The emitter density during the voltage rise phase produces a significant displacement at 0.7 volts, with a peak around  $40^\circ$  (dashed line); when the voltage falls back to 0.4 volts, the emitter density returns to its original distribution, and the total number of emitters is still lagging behind the potential. Although Fig. 2e shows the response of state-2 within one voltage cycle, this trend is preserved across repeated cycles. The observed change in the polar angle can be rationalized by the local polarization of the emitters. In addition, the widespread presence of charged defects in the pristine h-BN<sup>64-68</sup>, and the state configurations lead to a rearrangement of the molecule-defect structure when electrons are extracted or injected into defects, changing the polar angle of emission dipoles from one to the other. Density Functional Theory (DFT) is used to suggest a possible structure associated with the emission dipole moment (**Supplementary section 4**). Since h-BN has mirror symmetry along the X-Y plane, the polar angle of the emission dipole is caused by the orientation of the pi orbital between carbon and nitrogen and is deviated by the charge number of h-BN defect.

### 2.3 Azimuth angle interacts with the crystal lattice

In this section, turning our attention to the azimuth angle of each emitter to study the interaction of organic molecules on the crystal lattice, taking advantage of the well-defined crystal lattice of h-BN. All localized emitters are rendered as pseudo-color maps and stacked over time based on the azimuth angle (Fig. 3a). The multiple orientations present in crystallographically locations demonstrate the heterogeneity of emitters, indicating that the hotspot either could provide few binding sites in one spot or that multiple binding sites exist but cannot be resolved, due to the resolution limit of SMLM ( $\sim 30$  nm). The azimuth angles of emitters in the four regions of interests (ROIs) can be plotted as short sticks. Three of the ROIs are sharp crystal edges and one is a line defect. These dipoles are not exactly regulated into the same orientation by the crystal edges, where

ROI-1, 3, and 4 are at angles to the boundary, and ROI-2 is oriented coinciding with the direction of the crystal edge. However, when we plot the histogram of the  $\Delta\phi=|\phi_{\text{edge}}-\phi_{\text{emitters}}|$ , these angles are nicely concentrated in three groups (median: 74.5°, 18.3°, and 45.9°, respectively) and are radially spaced apart from each other. When we compare the box plots in Fig. 3d, the interquartile range of ROI-4 (17.6°) is significantly smaller than that of ROI-3 (43.2°) even though the directions of the two regions are parallel, which can be explained by reasoning that the line defect confines the dipoles more than the open edge. The larger width of the box plot for ROI-2 is understood in that two peaks exist in Fig. 3c. The respective proportions of the three states in each ROI are  $P1 \gg P2 > P3$ , while the fraction of the state-3 is almost negligible in these areas (Fig. 3e), compared to the flat area (dash line). This suggests that although crystal edges provide more contact opportunities for molecules and defects (i.e. the edges are brighter than the center in both SMLM and widefield results), rotational binding sites cannot be guaranteed because of the missing symmetry of the h-BN crystal at the edges.

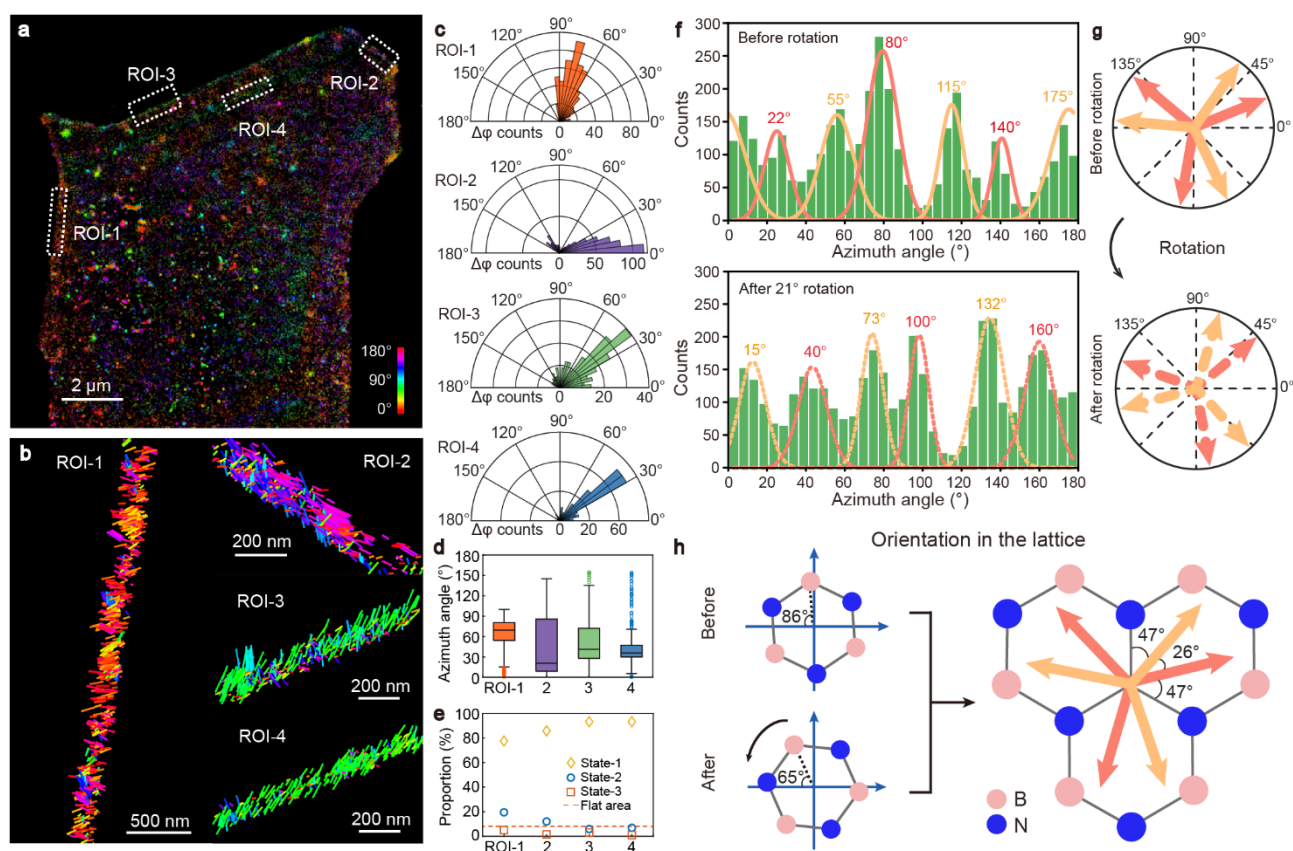


**Fig. 3 Azimuth angle of emitters on the h-BN surface.** (a) The SMLM image is rendered according to azimuth angle of emitters and temporally stacked; (b) Zoomed-in view of the four regions of interest in (a) with the azimuthal orientation marked with sticks and colors; (c) the angular distribution of  $\Delta\phi=|\phi_{\text{edge}}-\phi_{\text{emitters}}|$  in four ROIs; (d) Boxplot of four ROIs; (e) The fraction of the three states at the edge of the crystal ( $P1+P2+P3=1$  in each ROI) and the dashed line is the share of state-3 in the flat region. (f) Azimuth histogram of the state-2 emitters in the flat crystal area. Top: Before rotation, Bottom: After 21° horizontal rotation. (g) Azimuthal angles are restored to full space based on crystal symmetry. (h) Superposition of the azimuthal angle of the emitters with the crystal lattice.



We further examine the cluster of state-2 in the flat crystal area for which the azimuthal angle is most accurate, because the rotation-limited model considers the average orientation of the dipole, and thus dipole wobble will weaken the azimuthal accuracy significantly. The angular distribution of the  $12 \times 12 \mu\text{m}^2$  area in the flat center of the flake exhibits six distinct peaks and can be grouped into two clusters (Fig. 3f), where they are marked in red and orange separately. And when the sample was rotated about  $21^\circ$  (**Supplementary section 5**), the position of the azimuthal distribution moved the same as well. Then according to the symmetry of the h-BN structure, the orientation defined at  $0^\circ - 180^\circ$  can be further recovered to  $0^\circ - 360^\circ$  in the full space (Fig. 3g) and overlapped with the crystal lattice in Fig. 3h. Remarkably, we now readily find that the azimuthal angle does not strictly follow the h-BN structure, where the averaged orientation is  $47^\circ \pm 5^\circ$  (median  $\pm$  standard deviation) with respect to the lattice and the angle of the two symmetric clusters is  $26^\circ \pm 7^\circ$ . This symmetrical misalignment further emphasizes that the origin of these quantum emitters is the interaction of organic molecules with defects.

## 2.4 Molecule dynamics at solid-liquid interface

Interfacial fluorescent emitters are more dynamic than their solid-state counterparts and 2D materials are ideal platforms for single-molecule tracking due to their specific adsorption capacity for molecules and appropriate kinetic temporal scales<sup>13,15,16,21</sup>. We selected  $2 \times 10^5$  localizations in  $4 \times 10^3$  frames within a  $12 \times 12 \mu\text{m}^2$  flat region at the center of the crystal, and  $3 \times 10^4$  trajectories to obtain reliable statistical results. Fig. 4(a) shows a trajectory map for events longer than four consecutive frames, which are connected based on the localization of random active emitters with nanometric precision (see Methods Section Trajectory linking and analysis). These connected events show two main types: random walking on the crystal surface and trapping into hot spots by a fixed location, which is discriminated according to the probability density function (PDF) of the one-dimensional displacements shown in Fig. 4(b). These PDFs can always be represented by a superposition of two Gaussian models with increasing delay times ( $\tau$ ). The narrowed Gaussian with a constant standard deviation of 30 nm represents the trapped event, while the broader part with an increased standard deviation represents the trajectories of random walk. The diffusion coefficient of these emitters in trajectory is  $7.02 \times 10^{-14} \text{ m}^2/\text{s}$ . The dwell times of the trapped event and the trajectory follow the double exponential decay as Fig. 4(c), and the time constants that correspond to chemisorption are 35 ms and 68 ms, respectively. The inset shows that the traveling distance of trajectory events is significantly longer than trapped events. However, these emitters do not exhibit significant axial motion because of the attraction of h-BN crystals in Fig. 4(d) (**Supplementary section 6**).

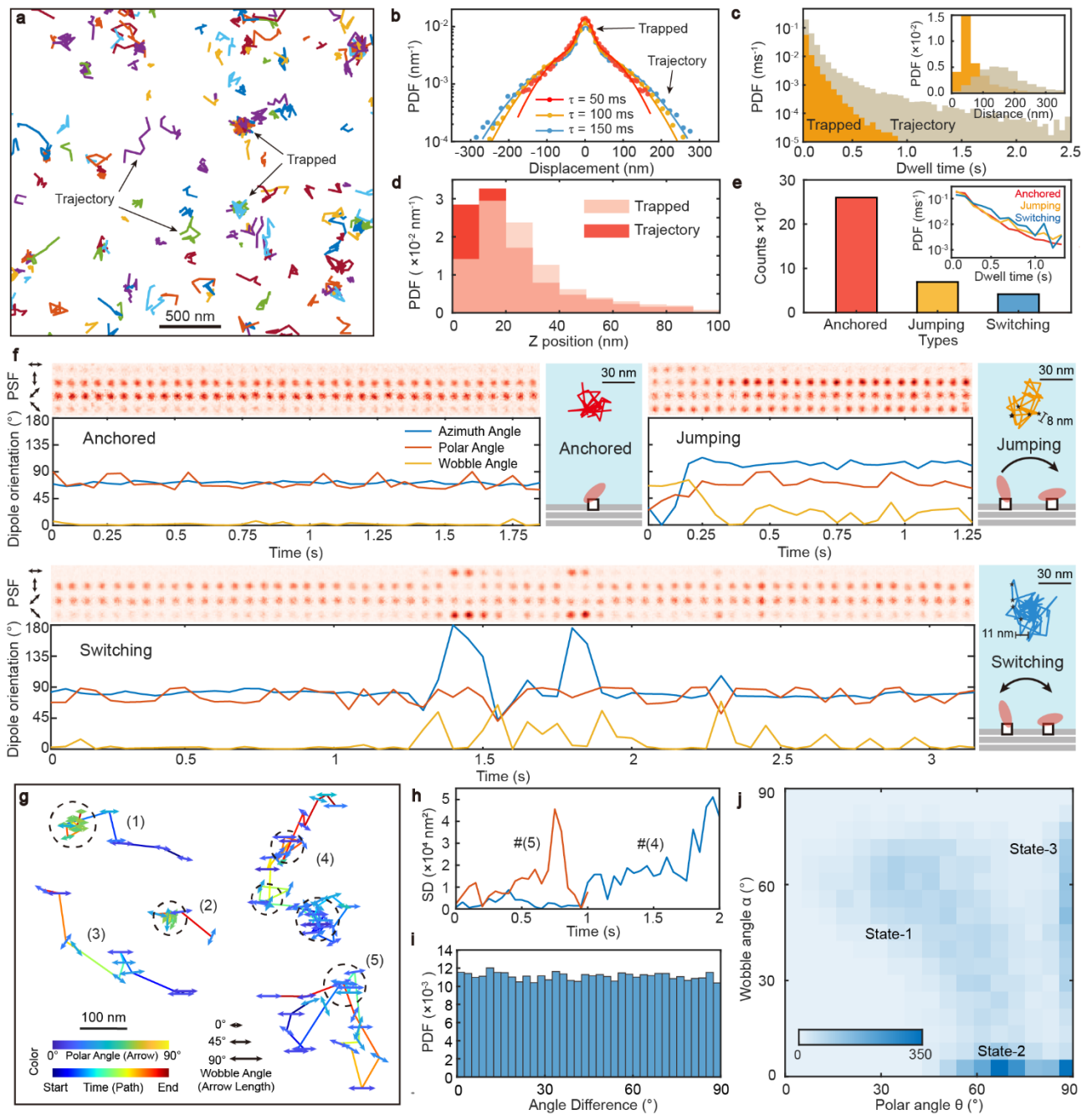


**Fig. 4 Molecule dynamics at solid-liquid interface.** (a) Trajectory map of events that are longer than 4 frames (200 ms). (b) The 1D displacement of all events with different lag time: 50 ms, 100 ms, and 150 ms. (c) The dwell time for trapped and trajectory events. The insert figure shows the distribution of traveling distance for two types of events. (d) The Z-position of trapped emitters and walking emitters. (e) Counts and fractions of three subcategories in the trapped event. The inserted figure shows the dwell time for the three subcategories of trapped events. (f) Three subcategories of trapped events: Anchored, jumping and switching. In the left panel of each event are the experimental PSFs and the fitted dipole orientation. In the right panel is the 2D trajectory and schematic illustration. (g) Three basic trajectory events and their combination. The orientation of the arrow indicates the azimuth angle of the emitters, the color indicates the polar angle and the length indicates the wobble angle. (h) the square displacement (SD) of #4 and #5 in (h). (i) The histogram of

the angle difference between the trajectory direction and the azimuth angle of each emitter. (j) The 2D density plot shows that the emitter in state-2 dominates the trapped events.

The emitter dynamics so far have been limited to the analysis of localizations. But here we can extend the dimension of molecular diffusion by including orientational information, allowing us to further stratify the trapped events into anchored, jumping, and switching behaviors. Their respective percentages approximately follow the exponential distribution as shown in Fig. 4(e) and Fig. 4(f) shows typical examples of these events. The anchored denotation means that the orientation and mobility of the dipole remain constant when the emitter is continuously activated at a fixed location while the jumping denotation indicates that the orientation of the dipole changes significantly during successive activations. Finally, the event of switching means that the emitter, although trapped in a fixed position within the resolution of SMLM, switches back and forth between two equilibrium states. The inset in Fig. 4(e) shows that the dwell times of the three subgroups are close to each other and their dwell times are on the same order of magnitude. In addition, because the orientation of these emitters is changed from one state to another, then we interpret this as the alternate capture of individual molecules by neighboring defects rather than the reorientation in identical positions. When the position of one state has been marked (the star in the trajectory illustration in Fig. 4(f)) in each event, it provides the possibility of combining different states to further improve the SMLM resolution for samples without prior knowledge. The double localization<sup>69</sup> results of these two demonstration events show that the distances between the two neighboring defects are  $8 \pm 3$  nm and  $11 \pm 4$  nm respectively<sup>65,67</sup>.

Finally, we turn our attention back to the trajectories of the emitters, which also include three basic types, as shown in Fig. 4(g): (1) the molecule is captured after random walking; (2) captured before leaving and (3) wandering freely on the surface. The azimuth angle is represented by an arrow in the figure, the color of the arrow codes the polar angle, and the arrow length is the wobble angle. The three basic behaviors described above can be further combined into complex behaviors (4) and (5). The trajectory(4) indicates that the same molecule is captured by three different defects consecutively, while trajectory(5) is that a molecule is captured by the same defect multiple times. This can be validated by the squared displacement (SD) of Fig. 4(h), where the trapped positions are presented as platforms on the curve. In addition, the angular difference between the orientation of the dipole and the direction of movement is uniformly distributed, indicating that the movement of the dipole is mainly governed by Brownian motion instead of the crystal lattice and that the transition dipole moment does not affect the macroscopic motion of the molecule. For example, when we review the trajectory shown in Fig. 4(g), we find that the trapped emitter seems to have a relatively smaller wobble angle (short arrow) or a larger polar angle (green color of arrow). Drawing a 2D heat map of the trapped events then shows that the emitters captured in one region mostly belong to

state-2, while the freely moving emitters are more active as states-1 & state-3. This further validates the above observation that the degree of angular freedom is inversely correlated to capture events.

### **3. Conclusion**

In summary, 2D h-BN effectively slows down single-molecule dynamics, enabling the capture of dynamics on time scales suitable for single-molecule localization imaging. Utilizing this platform, we demonstrated that dipole orientation can reveal different molecular conformations that benefit from the structural environment of h-BN lattice. Our experiments show that the rotational mobility of emitters is highly sensitive to electrochemical conditions, and their 3D orientation has a significant preference for the lattice structure. Additionally, the solid-liquid interface offers extensive possibilities for single-molecule dynamics: emitters can remain confined, jump, and move laterally at binding sites on the h-BN surface. This combination of molecular conformation, dynamics, and orientation allows us to achieve real-time and large-scale readouts of equilibrium states at the molecular level, which are unmatched by bulk measurements. We aim to advance the understanding of chemical reactions at the single-molecule scale, enhance trace sensing in confined nanofluidics, and open up possibilities for advanced optical super-resolution imaging by enabling the simultaneous observation of molecular conformations and photophysical activity.

## **4. Methods**

### **4.1 Sample preparation**

The precision coverslips (CG15XH, Thorlabs) were sonicated in 2% Hellmanex III and rinsed with deionized water for residual impurities before being exposed to oxygen plasma (90 seconds, 100 W). Pristine h-BN flakes were exfoliated from high-quality crystals and then transferred to clean coverslips, which were left to stand for 24 hours to improve transfer efficiency. The sample was mounted on the homebuilt microscope and its surface was completely covered with acetonitrile solvent (99.9% purity). The sample chamber was rinsed twice with the same acetonitrile solvent to clean residues before imaging.

### **4.2 Imaging setup**

The 561nm laser is modulated into circularly polarized light (97% ellipticity) by a combination of a polarizer (LPVISE100-A, Thorlabs) and a quarter-wave plate (WPQ05M-561, Thorlabs), and then illuminates the sample with normal incidence. The experimental sample is fixed on the nano-positioning systems (Mad City Labs) by a customized sample stage. Fluorescence is collected by a 60x, 1.42NA oil immersion objective lens (PLAPON60XO, Olympus), which performs well for polarization imaging. Excitation light around 561 nm wavelength is reflected by the dichroic mirror (Di03-R561-t1, Semrock), and the fluorescence from the sample is further filtered out by a

combination of low-pass (750nm, to remove the fluorescence from boron vacancy) and notch filters (561nm, to clean the reflected light from excitation beam). The variable waveplate (LCC1223-A, Thorlabs) is used for compensating the phase distortion caused by the birefringence and transmission coefficient difference of the first dichroic mirror coating. After the tube lens, a 50:50 non-polarizing beam splitter (BS016, Thorlabs) splits the fluorescence into two channels, and the polarization state of one path is rotated 45 degrees by the half-wave plate (AHWP10M-580, Thorlabs), and then two polarizing beam splitters (PBS251, Thorlabs) split them into four channels. In order to introduce z-axis information and to take full advantage of the polarization properties, the PSF image of one redundant channel is out of focus by 150-200 nm compared to the other three channels. Finally, all beams are reflected by mirrors to sCMOS (Prime-95B, Photometrics) for imaging and the maximum FOV is about  $40 \times 40 \mu\text{m}^2$ .

### **4.3 Imaging detection and estimation algorithms**

The imaging strategy was performed in an out-of-focus mode at about 100 nm in the axial axis, and the images of the four channels were registered by affine transformation and localized. Subsequently, after the PSFs of the same dipole in each channel are taken out from the raw data and assigned together, dipoles with empty channels of more than two are deleted, which avoids mis-localization by intrinsic physical constraints. The azimuthal angle of the dipole is calculated directly from the difference in light intensity of each channel, and the polar and wobble angles are fitted simultaneously by the simulated annealing algorithm.

### **4.4 Trajectory linking and analysis**

When the localization of the emitter in two consecutive frames is less than a given distance threshold, these two emitters will be connected on the temporal sequence. For trapped events, this threshold is 32 nm, and the threshold for randomly walking trajectories is 125 nm. The distance threshold is set according to the full width at half maximum ( $\text{FWHM} \approx 2.355\sigma$  for a Gaussian distribution) of the probability distribution of one-dimensional displacements, so the confidence that the event originated from the same emitter is larger than 95.44% ( $2\sigma$ ). The pipeline used to identify the three subcategories of capture events is as follows: The first step is to identify if a reorientation has occurred using outliers and thresholds to determine if it belongs to an anchored event. Subsequently, jumping and switching events are further determined by comparing the difference between the dipole orientations at the beginning and the end of the event sequence.

## **5. Acknowledgments**

W.G., T.C., N.R., E.M. and A.R. acknowledge funding from the European Research Council (grant 101020445—2D-LIQUID), and was supported by the EPFL Center for Imaging through its 2022 Call for Interdisciplinary Projects in Imaging. K.W. and T.T. acknowledge support from JSPS KAKENHI

(grant nos. 20H00354, 21H05233 and 23H02052) and World Premier International Research Center Initiative (WPI), MEXT, Japan.

## 6. Contributions

A.R., W.G., and N.R. conceived and designed the experiments. W.G. built the microscope. W.G. performed h-BN experiments with suggestions from T.C., N.R. and E.M.. T.C performed the DFT simulation. W.G. programmed the code and analyzed the data. W.G. wrote the manuscript with the help of A.R. and input from all authors. K.W. and T.T. contributed the materials. A.R. supervised the project. All authors discussed the results and commented on the manuscript.

## 7. Author information

Laboratory of Nanoscale Biology, Institute of Bioengineering, School of Engineering, École Polytechnique Fédérale de Lausanne (EPFL), Lausanne, Switzerland

Wei Guo, Tzu-Heng Chen, Nathan Roncery, Eveline Mayner, Aleksandra Radenovic

Research Center for Materials Nanoarchitectonics, National Institute for Materials Science, Tsukuba, Japan

Kenji Watanabe, Takashi Taniguchi

## 8. Conflict of interest

The authors declare no conflict of interest.

## 9. References

- 1 Wöll, D. *et al.* Polymers and single molecule fluorescence spectroscopy, what can we learn? *Chem. Soc. Rev.* **38**, 313-328 (2009). <https://doi.org/10.1039/B704319H>
- 2 Serag, M. F., Abadi, M. & Habuchi, S. Single-molecule diffusion and conformational dynamics by spatial integration of temporal fluctuations. *Nat. Commun.* **5**, 5123 (2014). <https://doi.org/10.1038/ncomms6123>
- 3 Brinks, D. *et al.* Ultrafast dynamics of single molecules. *Chem. Soc. Rev.* **43**, 2476-2491 (2014). <https://doi.org/10.1039/C3CS60269A>
- 4 Huang, J. *et al.* Tracking interfacial single-molecule pH and binding dynamics via vibrational spectroscopy. *Sci. Adv.* **7**, eabg1790 (2021). <https://doi.org/doi:10.1126/sciadv.abg1790>
- 5 Zhao, J. *et al.* Ligand efficacy modulates conformational dynamics of the  $\mu$ -opioid receptor. *Nature* **629**, 474-480 (2024). <https://doi.org/10.1038/s41586-024-07295-2>
- 6 Brandenburg, B. & Zhuang, X. Virus trafficking – learning from single-virus tracking. *Nat. Rev. Microbiol.* **5**, 197-208 (2007). <https://doi.org/10.1038/nrmicro1615>

- 7 Zhou, W. *et al.* Resolving the Nanoscale Structure of  $\beta$ -Sheet Peptide Self-Assemblies Using Single-Molecule Orientation–Localization Microscopy. *ACS Nano* **18**, 8798-8810 (2024). <https://doi.org/10.1021/acsnano.3c11771>
- 8 Inglesby, M. K. & Zeronian, S. H. Diffusion coefficients for direct dyes in aqueous and polar aprotic solvents by the NMR pulsed-field gradient technique. *Dyes Pigm.* **50**, 3-11 (2001). [https://doi.org/https://doi.org/10.1016/S0143-7208\(01\)00035-3](https://doi.org/https://doi.org/10.1016/S0143-7208(01)00035-3)
- 9 Schwartz, J. *et al.* Imaging 3D chemistry at 1 nm resolution with fused multi-modal electron tomography. *Nat. Commun.* **15**, 3555 (2024). <https://doi.org/10.1038/s41467-024-47558-0>
- 10 Zhao, L. *et al.* Horizontal molecular orientation in solution-processed organic light-emitting diodes. *Appl. Phys. Lett.* **106** (2015). <https://doi.org/10.1063/1.4907890>
- 11 Smit, R., Tebyani, A., Hameury, J., van der Molen, S. J. & Orrit, M. Sharp zero-phonon lines of single organic molecules on a hexagonal boron-nitride surface. *Nat. Commun.* **14**, 7960 (2023). <https://doi.org/10.1038/s41467-023-42865-4>
- 12 Mouterde, T. *et al.* Molecular streaming and its voltage control in ångström-scale channels. *Nature* **567**, 87-90 (2019). <https://doi.org/10.1038/s41586-019-0961-5>
- 13 Ronceray, N. *et al.* Liquid-activated quantum emission from pristine hexagonal boron nitride for nanofluidic sensing. *Nat. Mater.* **22**, 1236-1242 (2023). <https://doi.org/10.1038/s41563-023-01658-2>
- 14 Fumagalli, L. *et al.* Anomalously low dielectric constant of confined water. *Science* **360**, 1339-1342 (2018). <https://doi.org/10.1126/science.aat4191>
- 15 Sülzle, J. *et al.* Label-Free Imaging of DNA Interactions with 2D Materials. *ACS Photonics* **11**, 737-744 (2024). <https://doi.org/10.1021/acsp Photonics.3c01604>
- 16 Shin, D. H. *et al.* Diffusion of DNA on Atomically Flat 2D Material Surfaces. *bioRxiv*, 2023.2011.2001.565159 (2023). <https://doi.org/10.1101/2023.11.01.565159>
- 17 Comtet, J. *et al.* Anomalous interfacial dynamics of single proton charges in binary aqueous solutions. *Sci. Adv.* **7**, eabg8568 (2021). <https://doi.org/doi:10.1126/sciadv.abg8568>
- 18 Comtet, J. *et al.* Direct observation of water-mediated single-proton transport between hBN surface defects. *Nat. Nanotechnol.* **15**, 598-604 (2020). <https://doi.org/10.1038/s41565-020-0695-4>
- 19 Szalai, A. M. *et al.* Real-Time Structural Biology of DNA and DNA-Protein Complexes on an Optical Microscope. *bioRxiv*, 2023.2011.2021.567962 (2023). <https://doi.org/10.1101/2023.11.21.567962>
- 20 Lan, L. *et al.* Phase-Dependent Fluorescence Quenching Efficiency of MoS<sub>2</sub> Nanosheets and Their Applications in Multiplex Target Biosensing. *ACS Appl. Mater. Interfaces* **10**, 42009-42017 (2018). <https://doi.org/10.1021/acsaami.8b15677>

- 21 Zhang, M. *et al.* Super-resolved Optical Mapping of Reactive Sulfur-Vacancies in Two-Dimensional Transition Metal Dichalcogenides. *ACS Nano* **15**, 7168-7178 (2021). <https://doi.org/10.1021/acsnano.1c00373>
- 22 Ivády, V. *et al.* Ab initio theory of the negatively charged boron vacancy qubit in hexagonal boron nitride. *npj Comput. Mater.* **6**, 41 (2020). <https://doi.org/10.1038/s41524-020-0305-x>
- 23 Aharonovich, I., Englund, D. & Toth, M. Solid-state single-photon emitters. *Nat. Photonics* **10**, 631-641 (2016). <https://doi.org/10.1038/nphoton.2016.186>
- 24 Tran, T. T., Bray, K., Ford, M. J., Toth, M. & Aharonovich, I. Quantum emission from hexagonal boron nitride monolayers. *Nat. Nanotechnol.* **11**, 37-41 (2016). <https://doi.org/10.1038/nnano.2015.242>
- 25 Haykal, A. *et al.* Decoherence of  $V_B$  spin defects in monoisotopic hexagonal boron nitride. *Nat. Commun.* **13**, 4347 (2022). <https://doi.org/10.1038/s41467-022-31743-0>
- 26 Choi, S. *et al.* Engineering and Localization of Quantum Emitters in Large Hexagonal Boron Nitride Layers. *ACS Appl. Mater. Interfaces* **8**, 29642-29648 (2016). <https://doi.org/10.1021/acsmi.6b09875>
- 27 Li, S. & Gali, A. Identification of an Oxygen Defect in Hexagonal Boron Nitride. *J. Phys. Chem. Lett.* **13**, 9544-9551 (2022). <https://doi.org/10.1021/acs.jpcllett.2c02687>
- 28 Mendelson, N. *et al.* Identifying carbon as the source of visible single-photon emission from hexagonal boron nitride. *Nat. Mater.* **20**, 321-328 (2021). <https://doi.org/10.1038/s41563-020-00850-y>
- 29 Chen, Y. *et al.* Generation of High-Density Quantum Emitters in High-Quality, Exfoliated Hexagonal Boron Nitride. *ACS Appl. Mater. Interfaces* **13**, 47283-47292 (2021). <https://doi.org/10.1021/acsmi.1c14863>
- 30 Li, S. X. *et al.* Prolonged photostability in hexagonal boron nitride quantum emitters. *Commun. Mater.* **4**, 19 (2023). <https://doi.org/10.1038/s43246-023-00345-8>
- 31 Glushkov, E. *et al.* Engineering Optically Active Defects in Hexagonal Boron Nitride Using Focused Ion Beam and Water. *ACS Nano* **16**, 3695-3703 (2022). <https://doi.org/10.1021/acsnano.1c07086>
- 32 Xu, X. *et al.* Creating Quantum Emitters in Hexagonal Boron Nitride Deterministically on Chip-Compatible Substrates. *Nano Lett.* **21**, 8182-8189 (2021). <https://doi.org/10.1021/acs.nanolett.1c02640>
- 33 Comtet, J. *et al.* Wide-Field Spectral Super-Resolution Mapping of Optically Active Defects in Hexagonal Boron Nitride. *Nano Lett.* **19**, 2516-2523 (2019). <https://doi.org/10.1021/acs.nanolett.9b00178>
- 34 Glushkov, E. *et al.* Waveguide-Based Platform for Large-FOV Imaging of Optically Active Defects in 2D Materials. *ACS Photonics* **6**, 3100-3107 (2019). <https://doi.org/10.1021/acsp Photonics.9b01103>



- 35 Glushkov, E. *et al.* Direct Growth of Hexagonal Boron Nitride on Photonic Chips for High-Throughput Characterization. *ACS Photonics* **8**, 2033-2040 (2021). <https://doi.org/10.1021/acsp Photonics.1c00165>
- 36 Dong, B. *et al.* Super-resolution spectroscopic microscopy via photon localization. *Nat. Commun.* **7**, 12290 (2016). <https://doi.org/10.1038/ncomms12290>
- 37 Zhang, Z., Kenny, S. J., Hauser, M., Li, W. & Xu, K. Ultrahigh-throughput single-molecule spectroscopy and spectrally resolved super-resolution microscopy. *Nat. Methods* **12**, 935-938 (2015). <https://doi.org/10.1038/nmeth.3528>
- 38 Zhanghao, K. *et al.* Super-resolution dipole orientation mapping via polarization demodulation. *Light Sci. Appl.* **5**, e16166-e16166 (2016). <https://doi.org/10.1038/lsa.2016.166>
- 39 Hafi, N. *et al.* Fluorescence nanoscopy by polarization modulation and polarization angle narrowing. *Nat. Methods* **11**, 579-584 (2014). <https://doi.org/10.1038/nmeth.2919>
- 40 Valades Cruz, C. A. *et al.* Quantitative nanoscale imaging of orientational order in biological filaments by polarized superresolution microscopy. *Proc. Natl. Acad. Sci. U.S.A.* **113**, E820-E828 (2016). <https://doi.org/doi:10.1073/pnas.1516811113>
- 41 Enderlein, J., Toprak, E. & Selvin, P. R. Polarization effect on position accuracy of fluorophore localization. *Opt. Express* **14**, 8111-8120 (2006). <https://doi.org/10.1364/OE.14.008111>
- 42 Oleksiievets, N. *et al.* Fluorescence lifetime DNA-PAINT for multiplexed super-resolution imaging of cells. *Commun. Biol.* **5**, 38 (2022). <https://doi.org/10.1038/s42003-021-02976-4>
- 43 Thiele, J. C. *et al.* Confocal Fluorescence-Lifetime Single-Molecule Localization Microscopy. *ACS Nano* **14**, 14190-14200 (2020). <https://doi.org/10.1021/acsnano.0c07322>
- 44 Bowman, A. J., Huang, C., Schnitzer, M. J. & Kasevich, M. A. Wide-field fluorescence lifetime imaging of neuron spiking and subthreshold activity in vivo. *Science* **380**, 1270-1275 (2023). <https://doi.org/doi:10.1126/science.adf9725>
- 45 Backer, A. S., Lee, M. Y. & Moerner, W. E. Enhanced DNA imaging using super-resolution microscopy and simultaneous single-molecule orientation measurements. *Optica* **3**, 659-666 (2016). <https://doi.org/10.1364/OPTICA.3.000659>
- 46 Sun, B., Ding, T., Zhou, W., Porter, T. S. & Lew, M. D. Single-Molecule Orientation Imaging Reveals the Nano-Architecture of Amyloid Fibrils Undergoing Growth and Decay. *Nano Lett.* **24**, 7276-7283 (2024). <https://doi.org/10.1021/acs.nanolett.4c01263>
- 47 Zhang, O. *et al.* Six-dimensional single-molecule imaging with isotropic resolution using a multi-view reflector microscope. *Nat. Photonics* **17**, 179-186 (2023). <https://doi.org/10.1038/s41566-022-01116-6>

- 48 Rimoli, C. V., Valades-Cruz, C. A., Curcio, V., Mavrikis, M. & Brasselet, S. 4polar-STORM polarized super-resolution imaging of actin filament organization in cells. *Nat. Commun.* **13**, 301 (2022). <https://doi.org/10.1038/s41467-022-27966-w>
- 49 Ohmachi, M. *et al.* Fluorescence microscopy for simultaneous observation of 3D orientation and movement and its application to quantum rod-tagged myosin V. *Proc. Natl. Acad. Sci. U.S.A.* **109**, 5294-5298 (2012). <https://doi.org/doi:10.1073/pnas.1118472109>
- 50 Mehta, S. B. *et al.* Dissection of molecular assembly dynamics by tracking orientation and position of single molecules in live cells. *Proc. Natl. Acad. Sci. U.S.A.* **113**, E6352-E6361 (2016). <https://doi.org/doi:10.1073/pnas.1607674113>
- 51 Gould, T. J. *et al.* Nanoscale imaging of molecular positions and anisotropies. *Nat. Methods* **5**, 1027-1030 (2008). <https://doi.org/10.1038/nmeth.1271>
- 52 Zhang, O., Zhou, W., Lu, J., Wu, T. & Lew, M. D. Resolving the Three-Dimensional Rotational and Translational Dynamics of Single Molecules Using Radially and Azimuthally Polarized Fluorescence. *Nano Lett.* **22**, 1024-1031 (2022). <https://doi.org/10.1021/acs.nanolett.1c03948>
- 53 Backlund, M. P. *et al.* Simultaneous, accurate measurement of the 3D position and orientation of single molecules. *Proc. Natl. Acad. Sci. U.S.A.* **109**, 19087-19092 (2012). <https://doi.org/doi:10.1073/pnas.1216687109>
- 54 Curcio, V., Alemán-Castañeda, L. A., Brown, T. G., Brasselet, S. & Alonso, M. A. Birefringent Fourier filtering for single molecule coordinate and height super-resolution imaging with dithering and orientation. *Nat. Commun.* **11**, 5307 (2020). <https://doi.org/10.1038/s41467-020-19064-6>
- 55 Hulleman, C. N. *et al.* Simultaneous orientation and 3D localization microscopy with a Vortex point spread function. *Nat. Commun.* **12**, 5934 (2021). <https://doi.org/10.1038/s41467-021-26228-5>
- 56 Thorsen, R. Ø., Hulleman, C. N., Rieger, B. & Stallinga, S. Photon efficient orientation estimation using polarization modulation in single-molecule localization microscopy. *Biomed. Opt. Express* **13**, 2835-2858 (2022). <https://doi.org/10.1364/BOE.452159>
- 57 Mayner, E. *et al.* Monitoring electrochemical dynamics through single-molecule imaging of hBN surface emitters in organic solvents. *arXiv preprint arXiv:2405.10686* (2024).
- 58 Zhang, O. & Lew, M. D. Quantum limits for precisely estimating the orientation and wobble of dipole emitters. *Phys. Rev. Res.* **2**, 033114 (2020). <https://doi.org/10.1103/PhysRevResearch.2.033114>
- 59 Zhang, O. & Lew, M. D. Fundamental Limits on Measuring the Rotational Constraint of Single Molecules Using Fluorescence Microscopy. *Phys. Rev. Lett.* **122**, 198301 (2019). <https://doi.org/10.1103/PhysRevLett.122.198301>

- 60 Backer, A. S. & Moerner, W. E. Determining the rotational mobility of a single molecule from a single image: a numerical study. *Opt. Express* **23**, 4255-4276 (2015). <https://doi.org/10.1364/OE.23.004255>
- 61 Backer, A. S. & Moerner, W. E. Extending Single-Molecule Microscopy Using Optical Fourier Processing. *J. Phys. Chem. B* **118**, 8313-8329 (2014). <https://doi.org/10.1021/jp501778z>
- 62 Descloux, A., Grußmayer, K. S. & Radenovic, A. Parameter-free image resolution estimation based on decorrelation analysis. *Nat. Methods* **16**, 918-924 (2019). <https://doi.org/10.1038/s41592-019-0515-7>
- 63 Yang, Y. *et al.* Electrochemically controlled blinking of fluorophores for quantitative STORM imaging. *Nat. Photonics* (2024). <https://doi.org/10.1038/s41566-024-01431-0>
- 64 Yu, M., Yim, D., Seo, H. & Lee, J. Electrical charge control of h-BN single photon sources. *2D Mater.* **9**, 035020 (2022). <https://doi.org/10.1088/2053-1583/ac75f4>
- 65 Wong, D. *et al.* Characterization and manipulation of individual defects in insulating hexagonal boron nitride using scanning tunnelling microscopy. *Nat. Nanotechnol.* **10**, 949-953 (2015). <https://doi.org/10.1038/nnano.2015.188>
- 66 Wang, D. *et al.* Determination of Formation and Ionization Energies of Charged Defects in Two-Dimensional Materials. *Phys. Rev. Lett.* **114**, 196801 (2015). <https://doi.org/10.1103/PhysRevLett.114.196801>
- 67 Yang, Y. *et al.* Atomic Defect Quantification by Lateral Force Microscopy. *ACS Nano* **18**, 6887-6895 (2024). <https://doi.org/10.1021/acsnano.3c07405>
- 68 Wu, F., Galatas, A., Sundararaman, R., Rocca, D. & Ping, Y. First-principles engineering of charged defects for two-dimensional quantum technologies. *Phys. Rev. Mater.* **1**, 071001 (2017). <https://doi.org/10.1103/PhysRevMaterials.1.071001>
- 69 Reinhardt, S. C. M. *et al.* Ångström-resolution fluorescence microscopy. *Nature* **617**, 711-716 (2023). <https://doi.org/10.1038/s41586-023-05925-9>